REFERENCES

1. J. P. Hansen, *Phys. Rev. A* **8**, 3096 (1973); W. L. Slattery, G. D. Doolen, and H. E. DeWitt, *ibid.* **21**, 2089 (1980); **26**, 2255 (1982).
2. H. E. DeWitt and W. B. Hubbard, *Astrophys. J.* **168**, 131 (1976).
3. H. Totsuji and K. Tokami, *Phys. Rev. A* **30**, 3175 (1984).
4. F. J. Rogers, D. A. Young, H. E. DeWitt, and M. Ross, *Phys. Rev. A* **28**, 2990 (1983).
5. N. W. Ashcroft and D. Stroud, *Solid State Phys.* **33**, 2 (1978).
6. N. March and A. Murray, *Phys. Rev. A* **120**, 830 (1961); *Proc. R. Soc. London, Ser. A* **261**, 119 (1961).
7. H. L. Helfer, R. L. McCrory, and H. M. Van Horn, *J. Stat. Phys.* **37**, 577 (1984).

2.C Laser-Fusion-Target Implosion Studies with OMEGA

A major program to demonstrate the feasibility of direct-drive laser fusion is presently under way at LLE. A goal of this program is to compress deuterium-tritium (DT) fuel to 200 times its liquid density (200 XLD) by ablatively driving a target with the 24 UV (351-nm) beams of the 2-kJ OMEGA laser system. To reach these high fuel densities, targets consisting of cryogenically cooled fuel contained within thin shells of plastic or glass will be used.

Preliminary to the use of cryogenically cooled targets, numerical simulations have been performed[1,2] to identify target designs that would enable generation of high neutron yields and modest fuel densities (~50 XLD). Initial experiments on these types of targets have resulted in neutron yields of as much as 2×10^{11} (spring 1985) for high-yield targets and final densities of ~30 XLD for high-density targets.[3,4] These experiments provided the necessary conditions to test instrumentation that will be required to diagnose the performance of targets used in the 200-XLD campaign and to examine the performance of the targets relative to one-dimensional hydrodynamic code simulations.

In this report we summarize further direct-drive (high-yield) target implosion studies performed with the 24 UV (351-nm) beams of the 2-kJ OMEGA laser system (spring 1986). Targets consisted of glass microballoons (GMB) having initial aspect ratios ($R/\Delta R$) of ~200–300 and equimolar fills of deuterium and tritium at a pressure of 10 atm. Neutron yields as high as $\sim 3 \times 10^{11}$ were produced by accelerating these low-mass shells to high velocities, thereby producing core temperatures of ~5 keV and fuel densities of ~1 XLD. Diagnosis of

target performance during the acceleration phase of the target implosions was obtained from time- and space-resolved measurements of the x-ray emission from the laser-heated glass shells. Target performance during the deceleration or stagnation phase of the implosions was diagnosed by nuclear and particle instrumentation, from which estimates of total thermonuclear yield, fuel temperature, and fuel and shell densities were obtained.

The x-ray emission from the laser-heated glass microballoons was imaged by x-ray microscopes[5] and an imaging x-ray streak camera with an optical fiducial.[6] Plotted in Fig. 28.10 is the radius of the maximum x-ray emission versus time, determined from a streak camera image of a target implosion. Also plotted is the one-dimensional hydrodynamic-code *(LILAC)* predicted radius versus time, along with the idealized laser pulse, whose position was determined by reference to the optical fiducial. The measured radius of the target versus time, thus determined, follows the *LILAC* prediction fairly closely. However, the spatial distribution of the x-ray emission from time-integrated, x-ray microscope images shows departures from predictions; these departures correlate with initial target wall thickness. Figure 28.11 shows azimuthally averaged radial profiles determined from the x-ray images of a series of target implosions (including the example of Fig. 28.10). The targets in this series had almost the same initial radii but different wall thicknesses. The thinner-walled targets [Figs. 28.11(c) and 28.11(d)] produced time-integrated, radial x-ray profiles that deviated from the *LILAC*-predicted profiles by a larger extent than did the thicker-walled targets. However, the curve of the target radius versus time (determined from x-ray streak camera images) agreed with *LILAC* just as well for the thin-walled targets [Figs. 28.11(c) and 28.11(d)] as for the thick-walled targets [(Figs. 28.11(a) and 28.11(b)]. Simulations using *LILAC* show that such modified profiles occur if the intensity on the target is higher than that of the measured average value.

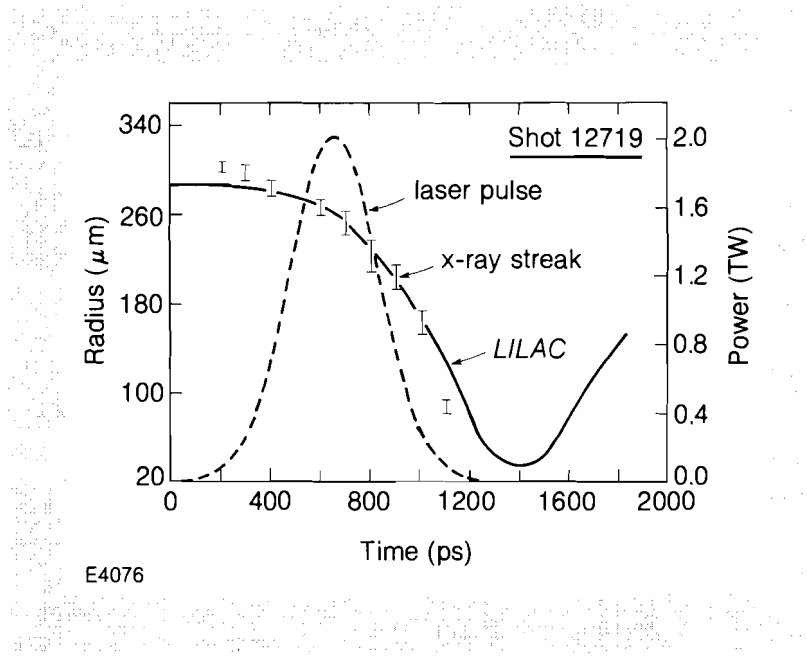

Fig. 28.10
The radius of the target versus time, as determined from the separation of the x-ray emission coming from opposite sides of the target, viewed by an x-ray streak camera with an imaging pinhole. LILAC *simulations of the same are also shown.*

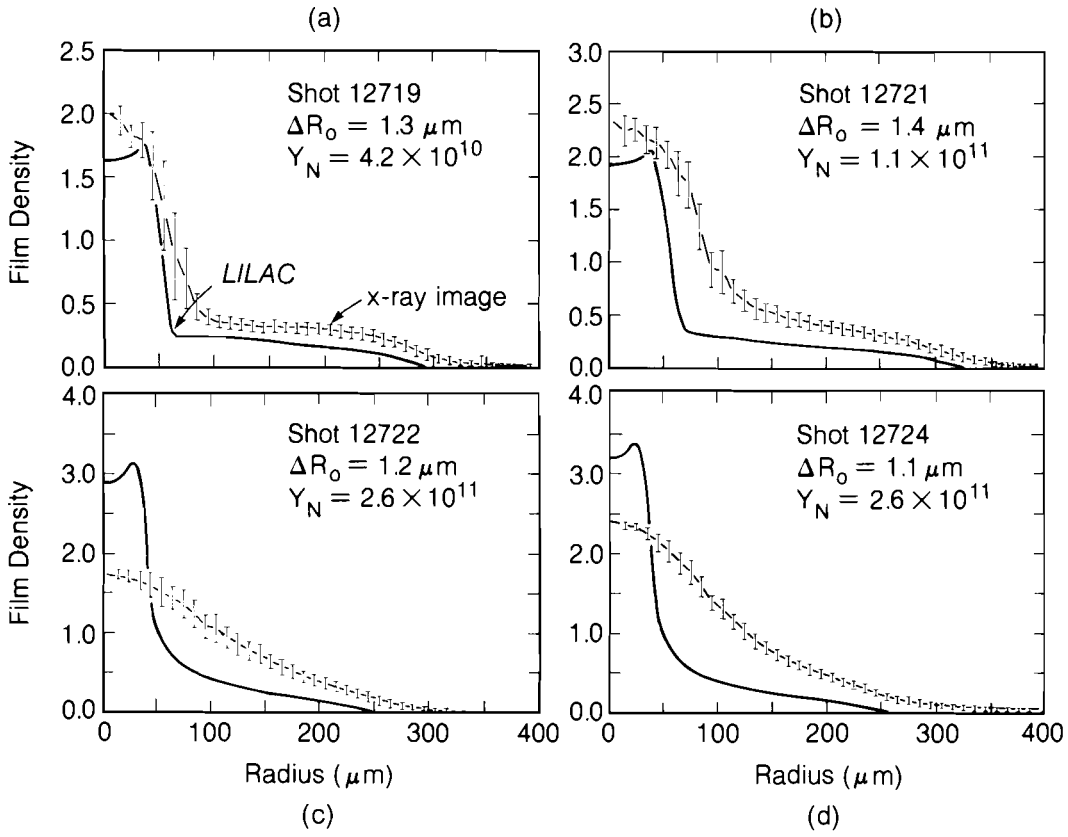

Fig. 28.11
Averaged radial profiles determined from time-integrated x-ray micrographs of target implosion. The LILAC *simulations take into account the response of the microscopes and film. (a) and (b) are examples of thicker shells; (c) and (d) are examples of thinner shells.*

Further indirect evidence of departures from predicted one-dimensional behavior that are more pronounced for thin-walled targets is seen in time-resolved, soft x-ray emission measurements made with a four-channel, 3-GHz, x-ray-diode spectrometer (MINIFLEX).[7] Figure 28.12 shows the time-resolved x-ray emission (around E ~1 keV) for the implosions of Fig. 28.11, as resolved by one of the fast x-ray photodiodes. *LILAC* simulations of the MINIFLEX response are also shown. The x-ray signal versus time is close to that predicted for the thicker-walled targets [Figs. 28.12(a) and 28.12(b)], the main features of which are emission coming from the glass shell during the laser pulse, and subsequent reheating of the shell, which occurs during the final stage of the implosion. The width of the stagnation peaks is significantly broader than the instrumental response time (~100 ps). The thinner-walled targets [Figs. 28.12(c) and 28.12(d)] show very little emission at the predicted time of stagnation, indicating that the shells had been

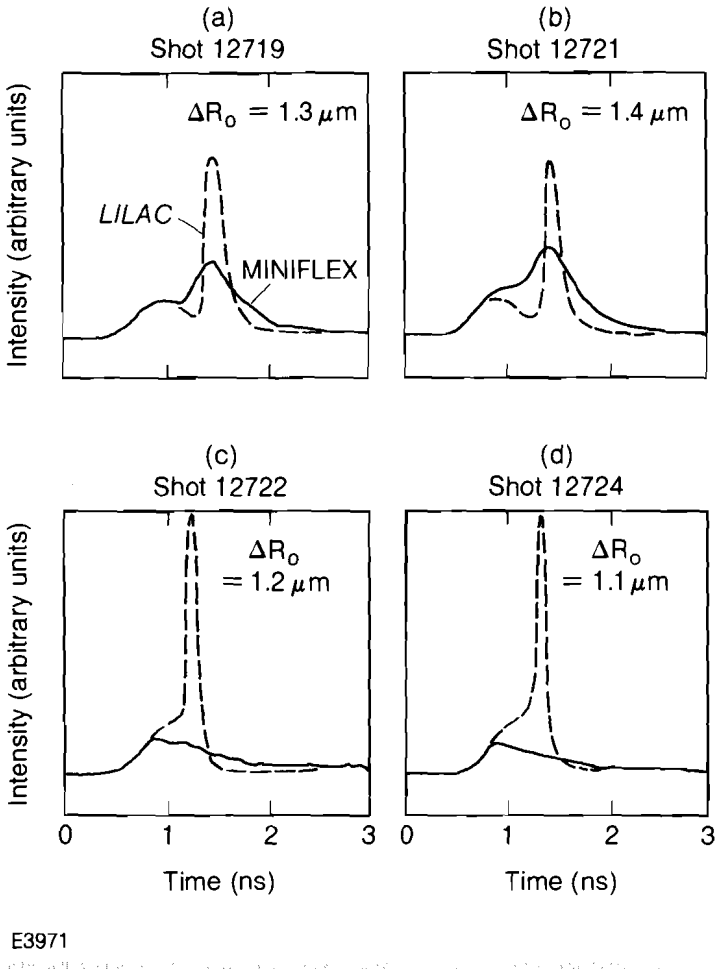

Fig. 28.12
Time-resolved, spatially integrated x-ray emission from the targets whose radial profiles are shown in Fig. 28.11, as resolved by the MINIFLEX system.

ablated away, had broken up, or had stagnated over a longer time. *LILAC* simulations of these implosions indicate that sufficient shell material in a thin shell should remain, so that a pronounced x-ray stagnation peak is predicted in all cases. In contrast, the shell radius versus time during the implosion appears to be correctly predicted by *LILAC* for the thinner-walled targets as well as for the thicker-walled targets, indicating that the predicted mass-ablation rate is close to the actual average mass-ablation rate. This points to something other than the average intensity (such as nonuniformities in the target illumination) as the cause for the apparent burn-through or breakup of shell material in the case of the thinner-walled targets.

The overall performance of the targets during the stagnation phase of the implosion is characterized by the neutron yield. Figure 28.13 shows the ratio of the measured and *LILAC*-predicted neutron yields versus the calculated convergence ratio. (The convergence ratio is defined as the ratio of the initial fuel radius divided by fuel radius of the stagnated core.) The result closest to the *LILAC*-predicted yield (~70%) was

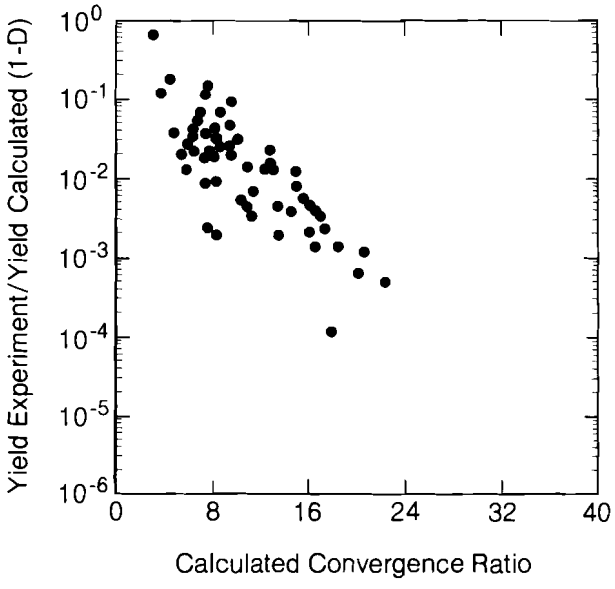

Fig. 28.13
Normalized neutron yield (ratio of experimentally measured neutron yield to calculated neutron yield) versus the calculated target convergence ratio (convergence ratio is defined as the ratio of the initial to the final target radius).

obtained for a target that had a calculated convergence ratio of only 3.2. As previously noted,[2] the declining agreement between measured and predicted neutron yields at higher predicted convergence ratios is an indication of the presence of implosion nonuniformities (which are estimated to be $\sigma_{rms} \sim 20\%$ for these experiments).

Time-integrated images of the alpha-particle emission were obtained by the technique of zone-plate imaging.[8,9] Figure 28.14(a) shows a composite of an x-ray image and alpha-particle image obtained on a single shot. Figure 28.14(b) shows equivalent one-dimensional profiles of these images, together with *LILAC*-predicted profiles. The extent of the alpha emission region is seen to lie within the *LILAC*-predicted x-ray emission profile, the latter being a good indicator of the predicted position of the shell material at stagnation. The alpha image profile (radially averaged) also matches the *LILAC*-predicted profile, although nonspherical features are seen in the image. The absolute magnitude of alpha-particle flux was normalized to the measured total neutron yield, which is smaller than the predicted value by a factor of 8.5. In general, the alpha emission region, where thermonuclear burning takes place, has a size comparable to that predicted. The alpha images indicate, however, that the burning region is not always spherically symmetric and sometimes there are several peaks in the alpha emission indicative of asymmetries in the imploded core. These asymmetries occur more often in the case of targets with thicker walls.

The fuel ion temperature (T_i) obtained during the time of thermonuclear burning was estimated by the technique of neutron time-

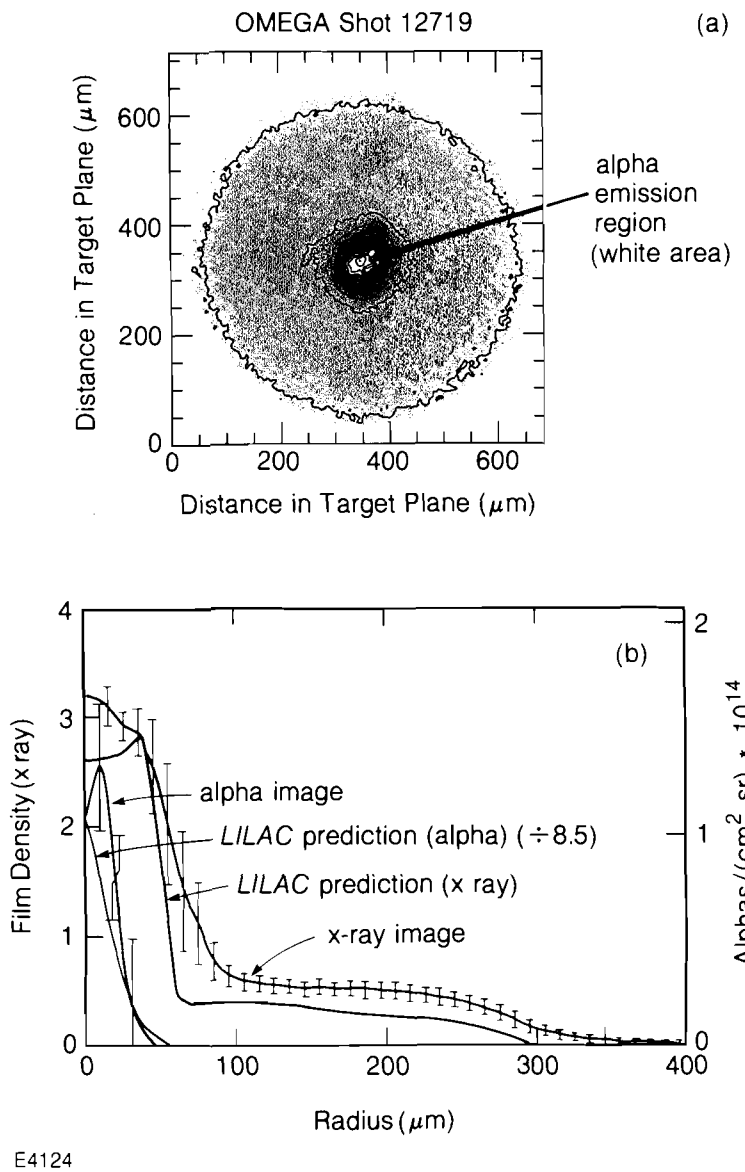

Fig. 28.14
(a) Composite of an x-ray micrograph (around E ~ 4 keV) of a high-yield target implosion and an alpha zone-plate image indicating the spatial distribution of the alpha particle products of thermonuclear burning.
(b) Averaged radial profiles of the images in (a), together with LILAC *postprocessor predictions of the same.*

of-flight (NTOF).[10] The NTOF-measured T_i for the target shots of Fig. 28.11 fall into two extremes. The thicker-walled targets [Figs. 28.11(a) and 28.11(b)] have NTOF-inferred T_i of 4.0 and 4.2 keV, respectively, as compared to *LILAC* predictions of 3.8 and 4.2 keV. The thinner-walled targets [Figs. 28.11(c) and 28.11(d)] have NTOF-inferred T_i of 10.9 and 14.4, while the *LILAC* predictions are 6.1 and 7.3 keV. The NTOF-inferred T_i are far in excess of the predicted temperatures for the thin-walled targets.

Two-dimensional hydrodynamic simulations of nonuniformly illuminated targets indicate[4] that at stagnation shell material may be

transported into the fuel, lowering T_i and decreasing the thermonuclear yield. Although inferred T_i for thin-walled targets appears higher than predicted (rather than lower), the increase in the width of the NTOF signal may be due to Doppler broadening by differential bulk motion of the fuel material, or by differences in ion temperature due to the existence of several separate burning regions. As an example, the 14.4-keV temperature inferred for shot 12724 could be explained by fuel in a burning shell that is moving radially inward at a velocity of $\sim 6 \times 10^7$ cm/s, a velocity comparable to the maximum velocity of the shell.

To summarize the measurements of target implosion behavior: (1) The average shell velocity appears to be well modeled in the acceleration phase of the implosion. However, velocity errors introduced by small-scale illumination nonuniformities may explain deviations from this average. (2) Measured, stagnated-shell sizes appear to agree more closely with *LILAC* calculations for those targets having thicker walls, although deviations from spherically symmetric implosions are evident. (3) Inferred T_i deviate from calculated T_i for those targets whose x-ray measurements are indicative of in-flight shell burn-through or breakup.

The NTOF-measured T_i, the $<\rho_f>$ inferred from alpha images, and the measured neutron yield Y_N can be compared for consistency by assuming that Y_N is given by

$$Y_N = \frac{n_{DT}^2}{4} <\sigma v> \tau_d V \quad , \tag{1}$$

where n_{DT} is the number density of DT pairs, $<\sigma v>$ is the velocity cross-section product averaged over the distribution of velocities, τ_d is the disassembly time, and V is the volume of the burn region. An estimate of the disassembly time is

$$\tau_d = R_f / C_s \quad , \tag{2}$$

where R_f is the radius and C_s is the sound speed, both pertaining to the burn region. The sound speed is given by

$$C_s = (\gamma_e P_e + \gamma_i P_i)^{1/2} \rho^{-1/2} \quad , \tag{3}$$

where γ is the ratio of specific heats, P_e and P_i are the electron and ion partial pressures, and ρ is the density.

Assuming $\gamma_e = \gamma_i = 5/3$ and $T_i \sim T_e$, the sound speed is given by

$$C_s = 3.6 \times 10^7 T_{keV}^{1/2} \text{ cm s}^{-1} \quad . \tag{4}$$

The DT-pair number density can be estimated by assuming that a fraction f of the fuel is confined to a region whose size is equal to the size of the alpha image, R_α:

$$n_{DT} = \rho_i f (R_i/R_\alpha)^3 / (m_D + m_T) \quad . \tag{5}$$

Taking the measured quantities of T_i, R_α, and Y_N and assuming $f \sim 1$ we can solve for the implied confinement time τ_d. Values of τ_d thus obtained are found to be of the order of a few picoseconds for the shots in Table 28.I. The values of the confinement time τ_d^*, calculated by assuming that the fuel is confined to a region of size R_α for one sound-speed crossing time, are listed in column 10 of Table 28.I. The yield-implied confinement times are seen to be unphysically small as compared to hydrodynamic time scales (i.e., the sound-speed crossing time). Alternatively, if we take the measured quantities of T_i, R_α, and Y_N and assume that the confinement time is given by τ_d^*, we can solve for the implied fraction of fuel, which is contributing to the burn. These values are given in column 11 of Table 28.I. In all cases the fuel contributing to burning is implied to be a small fraction of the original fuel mass.

Table 28.I
High-yield-target measured and derived quantities.

(1) Shot No.	(2) $R_i(\mu m)$	(3) $\Delta R_i(\mu m)$	(4) $E_{UV}(J)$	(5) Y_N (expt)	(6) Y_N *(LILAC)*	(7) T_i(keV) (expt)	(8) T_i(keV) *(LILAC)*	(9) $R_\alpha(\mu m)$	(10) τ_d^*(ps)	(11) f
12714	240.8	1.20	1223	8.7×10^{10}	2.7×10^{12}	–	–	45	–	–
12719	285.8	1.34	1235	4.2×10^{10}	3.4×10^{11}	4.0	3.8	53	61	0.32
12721	307.6	1.39	1342	1.1×10^{11}	7.1×10^{11}	4.2	4.2	52	56	0.38
12722	246.6	1.20	1404	2.6×10^{11}	2.7×10^{12}	10.9	6.1	55	42	0.33
12724	255.4	1.09	1465	2.6×10^{11}	3.7×10^{12}	14.4	7.3	49	22	0.21

(1) shot number; (2) initial target radius; (3) initial target wall thickness; (4) incident laser energy; (5) measured neutron yield; (6) *LILAC*-predicted neutron yield; (7) NTOF-inferred fuel ion temperature; (8) *LILAC*-predicted fuel ion temperature; (9) measured alpha-particle emission region size; (10) sound-speed crossing time of fuel region; (11) fraction of fuel partaking in thermonuclear burning, assuming burn has duration of τ_d^*.

E4086

We see that the measured values of T_i, R_α, and Y_N cannot be used to consistently describe, in a simple way, the thermonuclear burn that takes place in these experiments. Rather, mixing of fuel and shell material due to illumination nonuniformities may be causing a reduction in confined fuel mass, systematically high inferred ion temperatures as well as reduced burn times. Improvement in target performance in future experiments should be evidenced by more consistent measured values of T_i, R_α, and Y_N.

ACKNOWLEDGMENT

This work was supported by the U.S. Department of Energy Office of Inertial Fusion under agreement No. DE-FC08-85DP40200 and by the Laser Fusion Feasibility Project at the Laboratory for Laser Energetics, which has the following sponsors: Empire State Electric Energy Research Corporation, General Electric Company, New York State Energy Research and Development Authority, Ontario Hydro, Southern California Edison Company, and the University of Rochester. Such support does not imply endorsement of the content by any of the above parties.

REFERENCES

1. P. W. McKenty and C. P. Verdon, LLE Theory Group Report No. 15 (1985).
2. LLE Review **25**, 7 (1985).
3. LLE Review **24**, 161 (1985).
4. M. C. Richardson, P. W. McKenty, R. L. Keck, F. J. Marshall, D. M. Roback, C. P. Verdon, R. L. McCrory, J. M. Soures, and S. M. Lane, *Phys. Rev. Lett.* **56**, 2048 (1986).
5. M. C. Richardson, R. S. Marjoribanks, S. A. Letzring, J. M. Forsyth, and D. M. Villeneuve, *IEEE J. Quantum Electron.*, **QE-19**, 1861 (1983).
6. G. G. Gregory, S. A. Letzring, M. C. Richardson, and C. D. Kiikka, in *High Speed Photography, Videography, and Photonics III*, edited by B. G. Ponseggi and H. C. Johnson, (SPIE, Bellingham, WA, 1985), Vol. 569, p. 141.
7. LLE Review **25**, 20 (1986).
8. J. Wark (private communication).
9. N. M. Ceglio and L. W. Coleman, *Phys. Rev. Lett.* **39**, 20 (1977).
10. M. C. Richardson, P. W. McKenty, F. J. Marshall, C. P. Verdon, J. M. Soures, R. L. McCrory, O. Barnouin, R. S. Craxton, J. Delettrez, R. L. Hutchison, P. A. Jaanimagi, R. Keck, T. Kessler, H. Kim, S. A. Letzring, D. M. Roback, W. Seka, S. Skupsky, B. Yaakobi, and S. M. Lane, in *Laser Interaction and Related Plasma Phenomena Vol. 7*, edited by H. Hora and G. Miley (Plenum, New York, in press).